Cole–Hopf Transformed Solvers for Viscous Hamilton–Jacobi Reachability

Lekan Molu[a,1]

This manuscript was compiled on November 13, 2026

Viscous Hamilton–Jacobi (HJ) equations provide regularized value fields for backward reachability; however, their nonlinear gradient terms complicate numerical integration. We apply a variable-coefficient Cole–Hopf transformation that maps the viscous HJ equation to a semilinear heat equation. We integrate the complete transformed equation with periodic Fourier collocation and exponential Runge–Kutta time stepping, and with an independent fourth-order finite-difference scheme. Analytic solutions, grid and time refinement, coefficient variation, domain extension, and sampled equation residuals assess the numerical implementation. Rockets, relative-Dubins vehicles, a double integrator, and a starling-inspired relative-state model yield maximum sampled discrepancies between 5.60×10^{-4} and 3.223×10^{-3} against the corresponding reference fields. The resulting zero-sublevel geometries provide numerical topology diagnostics rather than continuum safety certificates. These experiments validate the transformed deterministic solvers on the stated grids and horizons.

Hamilton–Jacobi reachability | Cole–Hopf transformation | differential games | numerical partial differential equations | runtime safety assurance

Significance Statement

Hamilton–Jacobi reachability provides value fields for safety analysis, but nonlinear gradient terms complicate their numerical integration. A variable-coefficient Cole–Hopf transformation recasts the viscous equation as a semilinear heat equation when its complete nonlinear source is retained. Fourier and finite-difference solvers for the transformed equation agree with independent same-viscosity reference computations to within 3.3×10^{-3} on the reported observation queries. The comparisons establish numerical agreement on finite grids rather than continuum safety guarantees or sampling-based scalability. This separation clarifies which conclusions follow from the transformation, the deterministic discretizations, and repeated queries of a precomputed reduced-state field.

1. Introduction

Modern complex systems — with their diverse interconnection of actuators, sensors, control systems, and the software modules that coordinate their various processes and events — require software verification tools capable of geometrically reasoning about their future behaviors. Given the continuous and/or hybrid systems characterization of their dynamics, simulation and testing, verification, observation, and further testing loop cycles are the standard norm for detecting unforeseen behavior ahead of deployment. Owing to their scale, however, analyzing system behavior based on closed-form analytic mathematical tools is often infeasible. This has stimulated efforts that complement traditional mathematical analysis tools from dynamical systems with emerging techniques in reachability (1), viability (2), or invariance (3) theories. These new tools allow exploring all possible scenarios where faults may arise for safety assurance; that is, ascertaining the freedom of a system from harm by generating evidence that a system, or any its components satisfy all specified requirements including functional and allocated baselines (i.e., *verification*) (4). Examples of complex systems include smart manufacturing, ground (5) and air traffic management systems (6), flight control systems (7), or distributed systems.

Differential optimal control and game theories are useful formal verification tools for certifying the runtime safety assurance (3) of multiple agents interacting over a shared space in a *geometric* sense (8). Both rely on a resolution of the Hamilton-Jacobi-Bellman (HJB) and/or the Hamilton-Jacobi-Isaacs (HJI) equation (9). Being partial differential equations (PDEs), general high-dimensional HJB/HJI equations rarely admit closed-form solutions. Thus, approximation techniques have become the default mechanism for formal systems verification in these settings. Reachability theory (6, 10) is one such approximation technique. It entails computing the essentially non-oscillating (ENO) (11) Lax-Friedrichs (12) approximations to the HJ PDE via levelset methods (13–15). Propagating the fronts of a conservation law on a mesh, the inviscid Euler equations' solution reduces to the derivative of the HJ problem's solution (16); such that integrating this solution with total variation diminishing Runge-Kutta (TVD-RK) (17) produces generalized *viscosity solutions* to the original HJ problem.

HJ equation systems are employed within reachability analysis to evaluate a dynamical system's behavioral (or trajectory) evolution throughout a state space — for example, given its initial point sets (states). The problem is typically setup so that the initial set must satisfy *input or state constraints* in a *least restrictive sense* and under a *worst-possible disturbance* (18). Reachability is thus a useful

Author affiliations: [a]Molux Labs, LLC, Seattle, WA 98109

L.M. conceived the study, developed the analysis and software, performed the numerical experiments, and wrote the manuscript.

The author declares no competing interest.

[1]To whom correspondence should be addressed. Email: lekanmolu@scriptedonachip.com

DRAFT

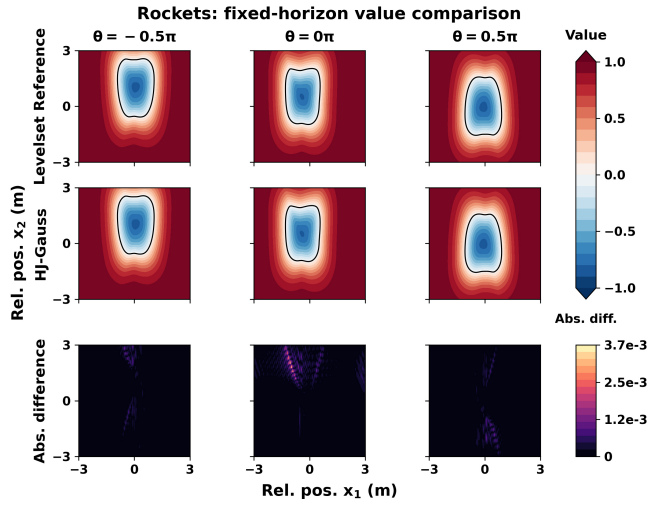


Fig. 1. Normalized rockets benchmark at elapsed horizon $T = 0.5$ and viscosity $\delta = 0.08$. Rows show the `Levelset` reference (14, 15), the transformed solver, and their absolute difference. Columns select the headings $\theta = -\pi/2$, 0, and $\pi/2$. Both solvers use the same initial condition, Hamiltonian, and viscosity. Black contours mark the zero level set of each fixed-horizon value.

geometric reasoning tool for determining the states that can be reached from an initial condition in a finite number of steps (10, 14) . *Reachability* can be analyzed in a (i) *forward* sense, where system trajectories are examined to determine if they enter certain states from an *initial set*; (ii) *backward* sense, where system trajectories are examined to determine if they enter certain *target sets*; (iii) *reach set* sense, in which they are examined to see if states reach a *set* at a *particular time*; or (iv) *reach tube* sense, in which they are examined to determine that they reach a set *during a time interval*.

This article studies the Cauchy equations associated with terminal reachability. A terminal reachable set concerns target entry at a fixed horizon; a tube permits entry during an interval and requires a stopping operator. Reach–avoid problems additionally constrain the trajectory before target entry and require an obstacle formulation. The reported experiments solve fixed-horizon viscous Cauchy problems. They do not compute a coupled population game or remove the tensor-grid dependence on state dimension.

Consider the evolution-form of the Cauchy-type HJ PDE

$$\begin{aligned} \boldsymbol{v}_t + \boldsymbol{H}(t;\boldsymbol{x},D\boldsymbol{v}) &= 0 && \text{in } \Omega\times(0,T], \\ \boldsymbol{v}(0;\boldsymbol{x}) &= \boldsymbol{g}(0;\boldsymbol{x}) && \text{on } \Omega\times\{t=0\} \end{aligned} \qquad \text{[HJ-IVP]}$$

where $\boldsymbol{x}\in\Omega\subseteq\mathbb{R}^n$, the Hamiltonian $\boldsymbol{H}$ is continuous, and $D\boldsymbol{v}$ is the spatial gradient. The initial condition $\boldsymbol{g}$ is bounded and uniformly continuous. Crossing characteristics can destroy classical differentiability even when the Hamiltonian and initial condition are smooth (19). Viscosity solutions provide generalized solutions. We study a fixed, positive-viscosity regularization before considering its approximation error.

We study a variable-coefficient Cole–Hopf transformation of the viscous form of Eq. (HJ-IVP). Positive logarithmic inversion maps the equation to a semilinear heat equation while retaining the Hamiltonian and coefficient derivatives. The transformed identity is analytical; the reported fields come from deterministic integration on periodic grids. Our results concern (i) the transformed source identity and logarithmic recovery formula; (ii) Fourier and finite-difference integration of the complete transformed equation; (iii) analytic, refinement, sensitivity, and same-viscosity reference comparisons; and (iv) a residual comparison result that applies when a uniform residual bound is available.

The numerical study does not invoke the dimension-independent complexity results for multilevel Picard methods (20). It also does not establish a continuum sign certificate from sampled residuals. The 100,000-state experiment interpolates one reduced relative-state field at independently sampled queries; population size affects the query count, not the dimension of the solved HJ equation.

Section 2 derives the transformed equation and describes the deterministic solvers. Section 3 reports analytic and game-based numerical comparisons. Appendix A records the heat-kernel representation, while Appendix B states the scope of the convergence and residual arguments. Section 4 concludes the paper.

2. Cole–Hopf Transformation and Deterministic Solvers

Backward reachability associates a differential game with a Hamilton–Jacobi–Isaacs equation (10). Let $\mathcal{U}\subset\mathbb{R}^m$ and $\mathcal{W}\subset\mathbb{R}^p$ be compact control sets. At physical time $s\in[0,T]$, let $\overline{\mathcal{U}}(s)$ and $\overline{\mathcal{W}}(s)$ contain the measurable control signals on $[s,T]$. Let $\mathcal{B}(s)$ contain the nonanticipative maps $\beta:\overline{\mathcal{U}}(s)\to\overline{\mathcal{W}}(s)$. The trajectory ξ starts in state $\boldsymbol{x}$ and satisfies

$$\dot{\xi}(r) = f\big(r,\xi(r),\boldsymbol{u}(r),\beta[\boldsymbol{u}](r)\big), \qquad \xi(s)=\boldsymbol{x}, \quad s\le r\le T, \tag{1}$$

where f is bounded, continuous and uniformly Lipschitz in $\boldsymbol{x}$. For bounded uniformly continuous running cost l and terminal cost $\boldsymbol{g}$, the lower value of the differential game is

$$\boldsymbol{v}_{\text{phys}}(s,\boldsymbol{x}) = \inf_{\beta\in\mathcal{B}(s)}\sup_{\boldsymbol{u}\in\overline{\mathcal{U}}(s)}\left\{\int_s^T l\big(r,\xi(r),\boldsymbol{u}(r),\beta[\boldsymbol{u}](r)\big)\,dr + \boldsymbol{g}(\xi(T))\right\}. \tag{2}$$

The target is represented by the zero sublevel set of $\boldsymbol{g}$. We assign $\boldsymbol{u}$ to the evader, which maximizes the payoff to avoid this set, and $\boldsymbol{w}$ to the pursuer, which minimizes the payoff to force target entry. The Hamiltonian is

$$\boldsymbol{H}_{\text{phys}}(s,\boldsymbol{x},\boldsymbol{p}) = \max_{\boldsymbol{u}\in\mathcal{U}}\min_{\boldsymbol{w}\in\mathcal{W}}\big\{\boldsymbol{p}\cdot f(s,\boldsymbol{x},\boldsymbol{u},\boldsymbol{w}) + l(s,\boldsymbol{x},\boldsymbol{u},\boldsymbol{w})\big\}. \tag{3}$$

For pure target-reach problems, the running cost is set to zero and the target is $\boldsymbol{g}$. The elapsed time $t=T-s$ converts the terminal condition into an initial condition so that if we write $\boldsymbol{v}(t,\boldsymbol{x}) = \boldsymbol{v}_{\text{phys}}(T-t,\boldsymbol{x})$ and define $\boldsymbol{H}(t,\boldsymbol{x},\boldsymbol{p}) = -\boldsymbol{H}_{\text{phys}}(T-t,\boldsymbol{x},\boldsymbol{p})$, the elapsed equation is $\boldsymbol{v}_t+\boldsymbol{H}(t,\boldsymbol{x},D\boldsymbol{v})=0$. Fixing $\delta>0$ gives the viscous parabolic regularization

$$\begin{aligned} \boldsymbol{v}^\delta_t + \boldsymbol{H}(t,\boldsymbol{x},D\boldsymbol{v}^\delta) &= \frac{\delta}{2}\Delta\boldsymbol{v}^\delta, \\ \boldsymbol{v}^\delta(0,\boldsymbol{x}) &= \boldsymbol{g}(\boldsymbol{x}). \end{aligned} \tag{4}$$

Equation Eq. (4) supplies approximation results under the Hamiltonian and initial condition (19, 21). The transformation below concerns classical solutions of this regularized equation.

DRAFT

Algorithm 1 Deterministic integration of the transformed equation

Choose $\delta > 0$, a prescribed smooth coefficient $\boldsymbol{c} \geq \boldsymbol{c}_- > 0$, a periodic box, and a time step Δt.
Discretize the box by Fourier collocation or centered finite differences.
Set $z^0 = \exp(-\boldsymbol{c}(0,\cdot)\boldsymbol{g})$.
for $j = 0, 1, \ldots, J-1$ **do**
    Reconstruct Dz^j and evaluate the complete source $F(t_j, \cdot, z^j, Dz^j)$.
    Advance diffusion and source terms by exponential Runge–Kutta or classical Runge–Kutta integration.
    Reject the step if the transformed field is nonfinite or nonpositive.
Recover the value from $\boldsymbol{v}^J = -\boldsymbol{c}(t_J, \cdot)^{-1} \log z^J$.

A. HJ Linearization. Write $\boldsymbol{v} = \boldsymbol{v}^\delta$ within this subsection and choose a prescribed coefficient $\boldsymbol{c} \in C_b^{1,2}([0,T] \times \mathbb{R}^n)$ with $0 < \boldsymbol{c}_- \leq \boldsymbol{c} \leq \boldsymbol{c}_+$. Define the transformed value and its initial condition by

$$\boldsymbol{\omega} = e^{-\boldsymbol{c}\boldsymbol{v}}, \qquad \boldsymbol{\omega}_0(\boldsymbol{x}) = e^{-\boldsymbol{c}(0,\boldsymbol{x})\boldsymbol{g}(\boldsymbol{x})}. \tag{5}$$

For a scalar $z > 0$ and vector $q \in \mathbb{R}^n$, introduce

$$V(t,\boldsymbol{x},z) = -\frac{\log z}{\boldsymbol{c}(t,\boldsymbol{x})},$$

$$P(t,\boldsymbol{x},z,q) = -\frac{q}{\boldsymbol{c}z} + \frac{\log z}{\boldsymbol{c}^2} D\boldsymbol{c}, \tag{6}$$

$$\boldsymbol{R}_{\mathrm{alg}}[\boldsymbol{c},V,P] = \boldsymbol{c}\left(\boldsymbol{H}(t,\boldsymbol{x},P) - \frac{\delta\boldsymbol{c}}{2}|P|^2\right), \tag{7}$$

$$\boldsymbol{R}_{\mathrm{der}}[\boldsymbol{c},V,P] = -\boldsymbol{c}_t V + \frac{\delta}{2}(\Delta\boldsymbol{c})V - \frac{\delta}{2}|D\boldsymbol{c}|^2 V^2 + \delta(1-\boldsymbol{c}V)D\boldsymbol{c}\cdot P, \tag{8}$$

$$F(t,\boldsymbol{x},z,q) = z\{\boldsymbol{R}_{\mathrm{alg}}[\boldsymbol{c},V,P] + \boldsymbol{R}_{\mathrm{der}}[\boldsymbol{c},V,P]\}. \tag{9}$$

Then, the transformed equation is

$$\begin{aligned} \boldsymbol{\omega}_t - \frac{\delta}{2}\Delta\boldsymbol{\omega} &= F(t,\boldsymbol{x},\boldsymbol{\omega},D\boldsymbol{\omega}), \\ \boldsymbol{\omega}(0) &= \boldsymbol{\omega}_0. \end{aligned} \tag{10}$$

For positive solutions, logarithmic inversion recovers the original viscous equation — reducing to a heat equation when the sum in Eq. (9) vanishes along the solution. Let S_t denote the heat semigroup with covariance $\delta t I_n$. The transformed equation admits the *mild representation*

$$\boldsymbol{\omega}(t) = S_t\boldsymbol{\omega}_0 + \int_0^t S_{t-s}F\big(s,\cdot,\boldsymbol{\omega}(s),D\boldsymbol{\omega}(s)\big)\,ds, \tag{11}$$

which couples values and gradients. Each mild update substitutes the preceding iterate into both source arguments.

For $f_k(s,\boldsymbol{x}) = F(s,\boldsymbol{x},z_k,Dz_k)$, the value and gradient update as an ordered pair:

$$(z_{k+1},Dz_{k+1})(t) = (S_t,DS_t)\boldsymbol{\omega}_0 + \int_0^t (S_{t-s},DS_{t-s})f_k(s)\,ds. \tag{12}$$

$$\begin{aligned} \boldsymbol{v}_{k+1}(t,\boldsymbol{x}) &= -\frac{\log z_{k+1}(t,\boldsymbol{x})}{\boldsymbol{c}(t,\boldsymbol{x})}, \\ D\boldsymbol{v}_{k+1} &= -\frac{Dz_{k+1}}{\boldsymbol{c}z_{k+1}} - \frac{\boldsymbol{v}_{k+1}}{\boldsymbol{c}} D\boldsymbol{c}. \end{aligned} \tag{13}$$

Appendix A derives the Gaussian forms of the source integral and coefficients. The numerical solvers integrate the complete transformed equation in time. They do not approximate the whole-interval Picard map by Monte Carlo sampling.

B. Fixed-horizon sets and reachable tubes. Let the target be the zero sublevel set

$$\mathcal{L}_0 = \{\boldsymbol{x} \in \mathbb{R}^n : \boldsymbol{g}(\boldsymbol{x}) \leq 0\}. \tag{14}$$

Under the value convention of Eq. (2), the zero sublevel set of the fixed-horizon solution identifies states from which the pursuer can force terminal target entry against the evader. The elapsed-time Cauchy equation is Eq. (4). This article computes that fixed-horizon field.

A backward reachable tube permits target entry before the terminal horizon. For an autonomous target-reach problem, its inviscid value satisfies a stopping equation of the form

$$\partial_t \boldsymbol{v}_{\mathrm{tube}} + \min\{0, \boldsymbol{H}(\boldsymbol{x}, D\boldsymbol{v}_{\mathrm{tube}})\} = 0, \qquad \boldsymbol{v}_{\mathrm{tube}}(0) = \boldsymbol{g}. \tag{15}$$

Reach–avoid problems require an additional obstacle condition (10). The stopping and obstacle equations are not used in the numerical comparisons below. We therefore reserve "tube" for this distinct formulation and call the computed objects fixed-horizon reachable sets.

Write $\boldsymbol{v} = \boldsymbol{v}^\delta$ in the transformation results that follow.

Lemma 2.1 (Transformation Identity)**.** *Suppose that* $\boldsymbol{v}(t;\boldsymbol{x}), \boldsymbol{c}(t;\boldsymbol{x}) \in C^{1,2}$ *and set* $\boldsymbol{\omega} = e^{-\boldsymbol{c}\boldsymbol{v}}$*. Define the residual* $r_v = \boldsymbol{v}_t + \boldsymbol{H}(t,\boldsymbol{x},D\boldsymbol{v}) - \delta\Delta\boldsymbol{v}/2$*. Then*

$$\boldsymbol{\omega}_t - \frac{\delta}{2}\Delta\boldsymbol{\omega} = \boldsymbol{\omega}\{\boldsymbol{R}_{\mathrm{alg}}[\boldsymbol{c},\boldsymbol{v},D\boldsymbol{v}] + \boldsymbol{R}_{\mathrm{der}}[\boldsymbol{c},\boldsymbol{v},D\boldsymbol{v}] - \boldsymbol{c}r_v\}. \tag{16}$$

Proof. Set $\phi = \boldsymbol{c}\boldsymbol{v}$. Differentiation gives $\boldsymbol{\omega}_t = -\boldsymbol{\omega}\phi_t$, $D\boldsymbol{\omega} = -\boldsymbol{\omega}D\phi$, and $\Delta\boldsymbol{\omega} = \boldsymbol{\omega}(|D\phi|^2 - \Delta\phi)$. Expand $D\phi = \boldsymbol{c}D\boldsymbol{v} + \boldsymbol{v}D\boldsymbol{c}$ and $\Delta\phi = \boldsymbol{c}\Delta\boldsymbol{v} + 2D\boldsymbol{c}\cdot D\boldsymbol{v} + \boldsymbol{v}\Delta\boldsymbol{c}$. Substitution cancels the two terms containing $\boldsymbol{c}\Delta\boldsymbol{v}$. The remaining terms give Eq. (16). Since $\boldsymbol{c}\boldsymbol{\omega} > 0$, the original residual vanishes if and only if the transformed residual vanishes. □

Corollary 2.1 (Homogeneous Heat Flow Reduction)**.** *Considering* Eq. (16)*, homogeneous heat flow holds if and only if* $\boldsymbol{R}_{\mathrm{alg}} + \boldsymbol{R}_{\mathrm{der}} = 0$*. A sufficient condition is a positive constant* $\boldsymbol{c}_0 > 0$ *and* $\boldsymbol{H}(t,\boldsymbol{x},D\boldsymbol{v}) := \delta\boldsymbol{c}_0|D\boldsymbol{v}|^2/2$*. The Hamiltonian* $\boldsymbol{H}(p) = |p|^2/2$ *satisfies this condition whenever* $\boldsymbol{c}_0 = 1/\delta$*.*

Proof. Apply Lemma 2.1 with $r_v = 0$. A constant $\boldsymbol{c}$ eliminates the derivative residual, and the quadratic relation eliminates the algebraic residual. □

Corollary 2.2 (Source representation and value recovery)**.** *Suppose* $\boldsymbol{\omega}_0$ *is bounded and uniformly continuous, and the source* $f(s,\boldsymbol{x}) = F(s,\boldsymbol{x},\boldsymbol{\omega}(s,\boldsymbol{x}),D\boldsymbol{\omega}(s,\boldsymbol{x}))$ *is bounded and*

DRAFT

continuous. Every bounded classical solution satisfies

$$\boldsymbol{\omega}(t,\boldsymbol{x}) = \mathbb{E}[\boldsymbol{\omega}_0(\boldsymbol{x}+\sqrt{\delta t}\,Z)] + \int_0^t \mathbb{E}[f(s,\boldsymbol{x}+\sqrt{\delta(t-s)}\,Z)]\,ds, \qquad [17a]$$

$$\boldsymbol{v}(t,\boldsymbol{x}) = -\frac{\log \boldsymbol{\omega}(t,\boldsymbol{x})}{\boldsymbol{c}(t,\boldsymbol{x})}, \qquad Z\sim\mathcal{N}(0,I_n). \qquad [17b]$$

Proof. Variation of constants for the heat equation gives the mild representation. The whole-space heat kernel has unit mass and equals the indicated Gaussian density. Invert the transformation at the evaluation point. □

The source contains the unknown solution. If $|\boldsymbol{v}| \le G$, then $e^{-\boldsymbol{c}+G} \le \boldsymbol{\omega} \le e^{\boldsymbol{c}+G}$.

Proposition 2.1 (Gradient for `HJ-Gauss`)**.** *Under the preceding bounded-source hypotheses, for $t>0$ the gradient satisfies*

$$D\boldsymbol{\omega}(t,\boldsymbol{x}) = \frac{\mathbb{E}[Z\boldsymbol{\omega}_0(\boldsymbol{x}+\sqrt{\delta t}\,Z)]}{\sqrt{\delta t}} + \int_0^t \frac{\mathbb{E}[Zf(s,\boldsymbol{x}+\sqrt{\delta(t-s)}\,Z)]}{\sqrt{\delta(t-s)}}\,ds, \qquad [18a]$$

$$D\boldsymbol{v}(t,\boldsymbol{x}) = -\frac{D\boldsymbol{\omega}(t,\boldsymbol{x})}{\boldsymbol{c}(t,\boldsymbol{x})\boldsymbol{\omega}(t,\boldsymbol{x})} - \frac{\boldsymbol{v}(t,\boldsymbol{x})}{\boldsymbol{c}(t,\boldsymbol{x})}D\boldsymbol{c}(t,\boldsymbol{x}). \qquad [18b]$$

Proof. Differentiate the Gaussian kernel with respect to its center. Its derivative has integrable L^1 norm bounded by $\sqrt{n/(\delta(t-s))}$. This bound justifies differentiation of the source integral. The product rule applied to $\boldsymbol{v} = -\boldsymbol{c}^{-1}\log\boldsymbol{\omega}$ gives the second formula. □

C. Deterministic discretizations. The Fourier solver represents the transformed field on a periodic tensor grid. Spectral differentiation supplies $D\boldsymbol{\omega}$, and a two-stage exponential Runge–Kutta update integrates diffusion and the complete nonlinear source. A one-third collocation cutoff suppresses unresolved source modes. The finite-difference solver instead uses fourth-order centered derivatives and classical fourth-order Runge–Kutta integration. Neither solver clips the transformed field; a nonpositive iterate terminates the computation.

The reference solver evolves the original viscous value equation. It uses fourth-order centered differences for the spectral comparisons and sixth-order centered differences for the finite-difference comparisons. These independent discretizations share the Hamiltonian, initial condition, viscosity, horizon, and observation queries. Their discrepancies measure agreement between the stated numerical schemes, not error relative to an unknown continuum solution.

The mild map also supplies a local analytical interpretation of the transformed equation.

Theorem 2.1 (Conditional finite-interval contraction)**.** *Let $X_\tau = C([0,\tau];\mathrm{BUC}^1)$ carry the sum of the uniform value and gradient norms. Suppose a nonempty closed set $\mathcal{A}\subset X_\tau$ is invariant under the mild map, its functions satisfy $a\le z\le b$ and $|Dz|\le Q$ with $a>0$, and the bounded source is uniformly Lipschitz in (z,Dz) with constant L. If*

$$\theta = L\left(\tau + 2\sqrt{n\tau/\delta}\right) < 1, \qquad [19]$$

then the mild map has a unique fixed point in $\mathcal{A}$. If that fixed point is classical, its logarithmic inverse solves the viscous Hamilton–Jacobi equation.

Appendix B proves the contraction statement. The deterministic time-stepping experiments do not verify its invariant-set hypotheses and do not use Picard iteration.

D. Residual and viscosity approximation errors. For a bounded smooth approximation U with bounded residual

$$r_U = U_t + \boldsymbol{H}(t,\boldsymbol{x},DU) - \frac{\delta}{2}\Delta U, \qquad [20]$$

comparison gives a value-error bound by the initial-condition error plus $\int_0^t \|r_U(s)\|_\infty ds$. If an independent vanishing-viscosity theorem also gives a bound $C_{\mathrm{vis}}\sqrt{\delta}$, the combined error bound is

$$E(t) = \|U(0)-\boldsymbol{g}\|_\infty + \int_0^t \|r_U(s)\|_\infty ds + C_{\mathrm{vis}}\sqrt{\delta}. \qquad [21]$$

The transformed residual satisfies $d = -\boldsymbol{c}\exp(-\boldsymbol{c}U)r_U$ (see Appendix B).

Corollary 2.3 (Conditional sign certification)**.** *Suppose $|U-\boldsymbol{v}^0|\le E$ on a specified set, with $\boldsymbol{v}^0\le 0$ denoting the target-reaching class. Then $U>E$ implies $\boldsymbol{v}^0>0$, and $U<-E$ implies $\boldsymbol{v}^0<0$. The remaining states form the abstention band $|U|\le E$.*

The proof is given in Appendix B.

3. Deterministic Validation and Population Queries

The experiments test the transformed solver's discretization accuracy and its use for repeated field queries. Each comparison shares the viscosity, Hamiltonian, bounded initial condition, and horizon. The resulting discrepancy therefore excludes viscosity bias but retains the numerical errors of both solvers. All recomputed fields use the elapsed-time convention of Section 2. The inherited raster figures label the comparison field "Ground Truth." In this manuscript, that label denotes the independent numerical reference and not the unknown continuum solution.

A. Starling-inspired relative-state geometry. The starling-inspired case tests repeated evaluation of a controlled relative-state field. It does not model a coupled flock trajectory. The solved state is $\boldsymbol{x} = (x_1, x_2, \theta)$, comprising two relative positions and one relative heading. Equal vertical control bounds cancel in the four-component physical Hamiltonian, while an altitude-independent terminal payoff gives $p_z = 0$. The four-component query state can therefore be evaluated through the reduced three-dimensional field.

For unit vehicle speeds and steering bounds, the elapsed-time Hamiltonian is

$$\boldsymbol{H}(\boldsymbol{x},p) = p_1(1-\cos\theta) - p_2\sin\theta - |p_1x_2 - p_2x_1 - p_3| + |p_3|. \qquad [22]$$

DRAFT

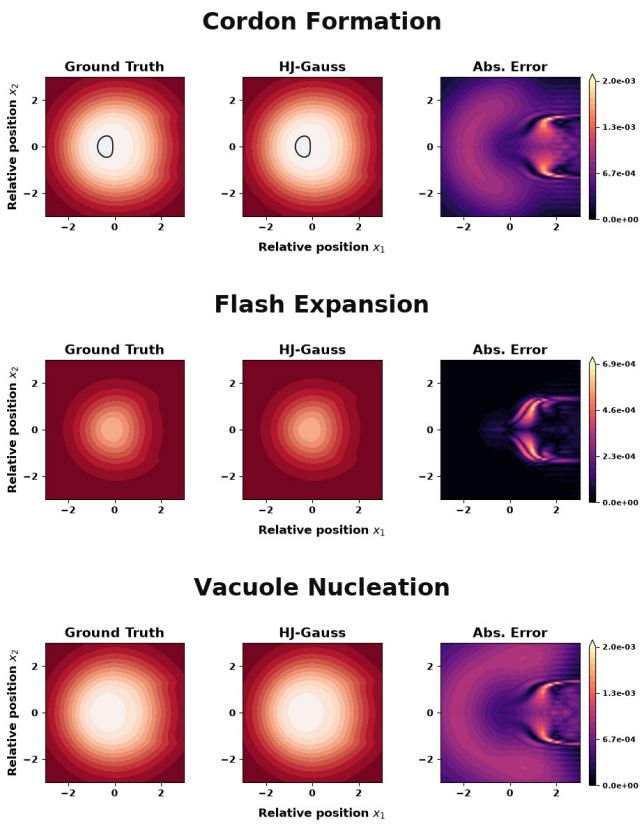


Fig. 2. Starling-inspired fixed-horizon values for three terminal-payoff configurations. Each group shows the reference field, transformed-solver field, and absolute difference. Black contours mark the zero level sets.

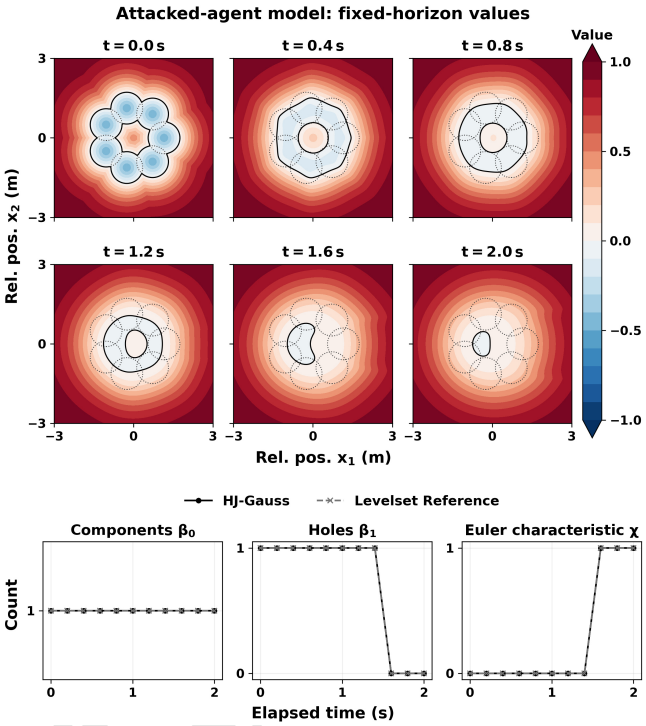


Fig. 3. Finite-window geometry of the starling-inspired value. Upper panels show six elapsed horizons, black zero contours, and dotted terminal disks. The lower panel reports component, hole, and Euler counts from thresholded numerical slices.

The baseline terminal payoff is the minimum of seven smoothed radial payoffs. Their centers lie on a ring of radius 1.15, and each target disk has radius 0.6. Taking the minimum forms the union of the seven terminal targets before evolution. This construction does not assert that independently optimized flock values commute with shared controls.

Figure 2 shows three terminal-payoff configurations used to visualize annular, expanding, and perforated zero-sublevel geometries. The labels connect the shapes to starling-inspired behavior. They are geometric descriptions, not biological or game-theoretic classification theorems.

A.1. Finite-window topology diagnostics. For a two-dimensional slice, let $n_{\mathrm{comp}}(t)$ be the number of connected components of the numerical zero sublevel set and let $\beta_1(t)$ count enclosed complementary components. The finite-window Euler diagnostic is

$$\chi(t) = n_{\mathrm{comp}}(t) - \beta_1(t). \qquad [23]$$

The implementation thresholds each saved slice, labels its connected components, and counts enclosed holes. Figure 3 reports these integer diagnostics for both numerical fields. Agreement of the two discretizations supports the displayed finite-grid geometry. It does not locate a continuum topology transition or prove a barrier certificate.

A.2. Population query experiment. A seeded cohort contains 100,000 independently sampled states. Horizontal positions are uniform on $[-3, 3]^2$, altitude is uniform on $[-1, 1]$, and heading is uniform on $[-\pi, \pi)$. Each query uses its horizontal position and heading to interpolate the same precomputed three-dimensional field; altitude is retained in the cohort record but does not enter the reduced solution. The experiment therefore measures the cost and consistency of repeated interpolation. It is not a joint 400,000-dimensional solve, a simulation of interacting birds, or a population-wide safety certificate.

Figure 4 displays 2,000 cohort states for legibility. The overlaid contour is the $\theta = 0$ slice, while each stored value uses the corresponding state's heading.

B. The Double Integrator Time-optimal Control Problem. The double-integrator benchmark asks which states can reach the origin under a bounded control (22, 23). With second-order dynamics $\ddot{\boldsymbol{x}} = \boldsymbol{u}$, the first-order state satisfies

$$\dot{\boldsymbol{x}}_1(t) = \boldsymbol{x}_2(t), \qquad \dot{\boldsymbol{x}}_2(t) = \boldsymbol{u}(t), \qquad |\boldsymbol{u}(t)| \le 1. \qquad [24]$$

The physical-time Hamiltonian is $\boldsymbol{H}_{\mathrm{phys}} = p_1\boldsymbol{x}_2 + p_2\boldsymbol{u}$. Minimization over the bounded control gives $\boldsymbol{u}^* = -\mathrm{sign}(p_2)$ for $p_2 \neq 0$. The elapsed-time Hamiltonian used by both numerical solvers is

$$\boldsymbol{H}(\boldsymbol{x}, p) = -p_1\boldsymbol{x}_2 + |p_2|. \qquad [25]$$

Figure 5 compares the transformed solution with the analytical time-to-origin geometry (14). The bottom row shows the absolute field discrepancy at each saved time. Table 2 reports a maximum sampled reference discrepancy

DRAFT

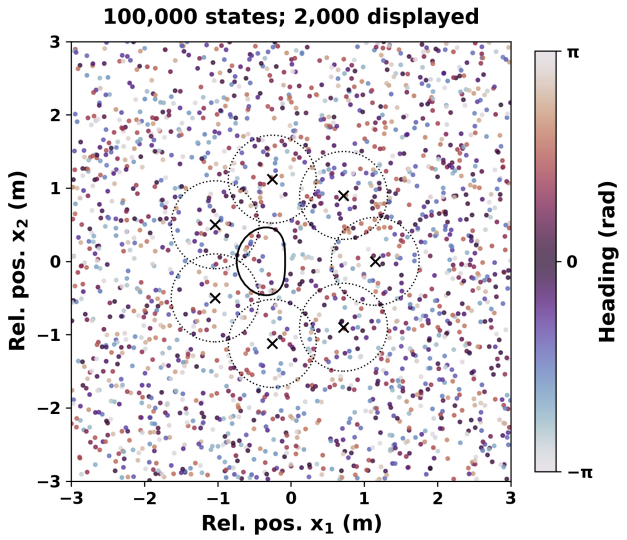


Fig. 4. Planar projection of 2,000 states from the 100,000-state query cohort. Color denotes heading. Crosses and dotted circles mark the seven target centers and terminal disks; the black contour is the $\theta = 0$ slice.

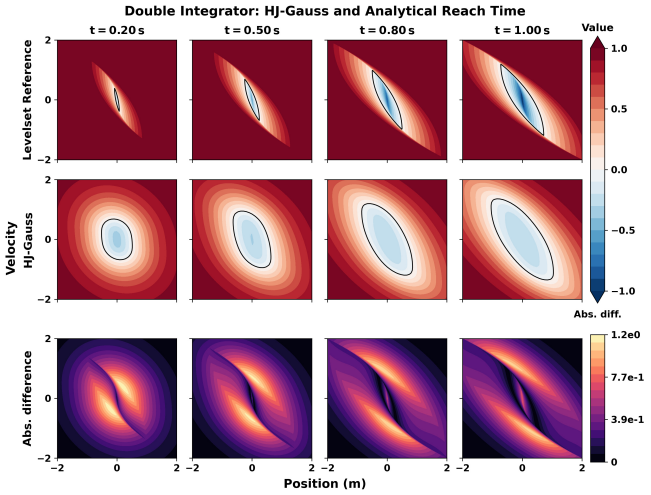


Fig. 5. Double-integrator values at four elapsed times with $\delta = 0.08$. Rows show the analytical reference, transformed-solver value, and absolute difference. Black contours mark the zero level sets in the first two rows.

of 5.60×10^{-4}; this field comparison does not establish set containment.

C. The Rockets Launch Problem on a Plane Benchmark. The planar rocket example of Dreyfus (24), recast as a differential game in (14), provides the next benchmark. Its relative dynamics are

$$\begin{aligned} \dot{x}_1 &= a\cos\theta + u_e x_1, \\ \dot{x}_2 &= a\sin\theta + a + u_p x_1 - g, \\ \dot{\theta} &= u_p - u_e. \end{aligned} \qquad [26]$$

The scalar g is gravitational acceleration, a is vehicle acceleration, and $\theta \in \mathbb{S}^1$ is the relative heading. The attitude-rate controls satisfy $u_e, u_p \in [-1, 1]$. The evader maximizes the terminal payoff, while the pursuer minimizes it. The elapsed-time Hamiltonian is (14)

$$\begin{aligned} \boldsymbol{H}(\boldsymbol{x}, p) = &-ap_1\cos\theta - p_2(g - a - a\sin\theta) \\ &- |p_1 x_1 - p_3| + |p_2 x_1 + p_3|, \end{aligned} \qquad [27]$$

The experiment sets $a = 1$, $g = 2$, capture radius 1.5, viscosity $\delta = 0.08$, and horizon $T = 0.5$. Figure 1 compares the transformed solver with the `LevelSetPy` reference (14, 15).

The terminal payoff is a smoothed signed-distance field for a cylindrical capture target. The three displayed headings use a shared color scale and observation window. Table 2 reports the maximum sampled field discrepancy, while Table 1 reports time-step, coefficient, and box sensitivity.

D. Dubins Vehicles Homicidal Chauffeur Problem. Merz's pursuit–evasion game extends the homicidal chauffeur problem to two vehicles with comparable speeds and turn radii (25, 26). The experiment computes terminal-horizon viscosity values. Let $\boldsymbol{x} = (x_1, x_2, x_3)$ be the pursuer's position and heading relative to an evader centered at the origin. With constant linear speeds $v_e, v_p > 0$ and steering rates $w_e, w_p \in [-w, w]$, the relative dynamics are (10)

$$\begin{aligned} \dot{x}_1 &= -v_e + v_p\cos x_3 + w_e x_2, \\ \dot{x}_2 &= v_p\sin x_3 - w_e x_1, \\ \dot{x}_3 &= w_p - w_e. \end{aligned} \qquad [28]$$

Set $v_e = v_p = w = 1$ so that for matched headings, identical steering signals preserve the initial separation. The capture target surface is the cylinder $\mathcal{T} = \{\boldsymbol{x} : x_1^2 + x_2^2 \le r^2\}$, with capture radius $r > 0$. In absolute coordinates, the dynamics is $\dot{x}_1 = \cos\theta$, $\dot{x}_2 = \sin\theta$, and $\dot{\theta} = u$, with $|u| \le 1$ and a pose target that includes heading. Write the Hamiltonian as $\boldsymbol{H} = -p_1\cos\theta - p_2\sin\theta + |p_3|$. The physical-time Hamiltonian $\boldsymbol{H}_{\text{phys}} = \max_{w_e}\min_{w_p} p \cdot f$ is

$$\begin{aligned} \boldsymbol{H}_{\text{phys}}(\boldsymbol{x}, p) = &\, p_1(v_p\cos x_3 - v_e) + p_2 v_p\sin x_3 \\ &+ w|p_1 x_2 - p_2 x_1 - p_3| - w|p_3|. \end{aligned} \qquad [29]$$

For the normalized bounds $v_e = v_p = w = 1$, the Hamiltonian becomes

$$\begin{aligned} \boldsymbol{H}_{\text{phys}}(\boldsymbol{x}, p) = &\, p_1(\cos x_3 - 1) + p_2\sin x_3 \\ &+ |p_1 x_2 - p_2 x_1 - p_3| - |p_3|. \end{aligned} \qquad [30]$$

For elapsed backward time, the numerical Cauchy problem uses $\boldsymbol{H} = -\boldsymbol{H}_{\text{phys}}$. For unit bounds this is

$$\begin{aligned} \boldsymbol{H}(\boldsymbol{x}, p) = &\, p_1(1 - \cos x_3) - p_2\sin x_3 \\ &- |p_1 x_2 - p_2 x_1 - p_3| + |p_3|. \end{aligned} \qquad [31]$$

The recomputed terminal-horizon fields use this Hamiltonian without a stopping operator.

The levelset comparison (14) with `HJ-Gauss` for the Dubins vehicles in relative coordinates is shown in Figure 6; Table 2 reports its refinement checks.

E. Numerical setup notes and hyperparameters. Algorithm 1 summarizes the implemented numerical procedure. For the rockets and relative-Dubins cases, the transformed solver uses second-order exponential Runge–Kutta time

DRAFT

Table 1. Maximum sampled changes under time halving, coefficient variation, isolated boundary extension, and combined box sensitivity. Boundary extension fixes the `Levelset` Reference time step, spacing, heading count, Hamiltonian, and initial condition on the common box.

System	Time	Coefficient	Combined box
Rockets	7.19×10^{-6}	1.84×10^{-4}	0.00136
Dubins vehicles	3.97×10^{-5}	2.79×10^{-5}	5.26×10^{-5}
Single Dubins	1.47×10^{-6}	1.02×10^{-5}	8.83×10^{-6}
Double integrator	6.85×10^{-7}	1.73×10^{-6}	4.40×10^{-5}
Bird model	6.23×10^{-7}	7.46×10^{-6}	5.46×10^{-4}

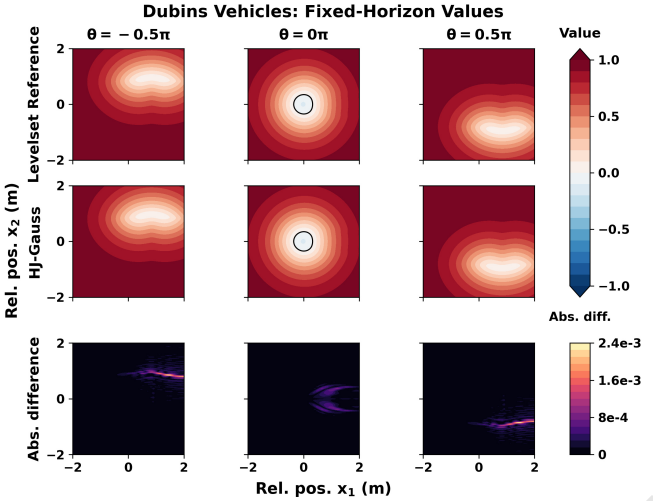


Fig. 6. Relative-Dubins terminal-horizon values at $T = 1$ and $\delta = 0.08$. Rows show the `Levelset` Reference (14), `HJ-Gauss`, and their absolute difference. Columns select three headings. Black contours mark the zero level set. The comparison uses the same Hamiltonian, initial condition, and viscosity in both solvers.

stepping on a periodic Fourier grid. A fourth-order finite-difference discretization with classical fourth-order Runge–Kutta integration evolves the original viscous equation. The starling-inspired case uses fourth-order centered differences and classical fourth-order Runge–Kutta integration for the transformed equation. Its reference uses sixth-order centered differences and fourth-order Runge–Kutta integration.

All figures assign the `levelset`scales $L_* = 1\,\mathrm{m}$ and $T_* = 1\,\mathrm{s}$, so that positions are displayed in meters and elapsed time in seconds. The Starlings example payoff takes the minimum of seven translated radial payoffs, with target centers on a radius-1.15 ring and disk radius 0.6. The baseline spatial box is $[-6, 6]^2$, with periodic heading $[-\pi, \pi)$ for three-dimensional cases. Completion makes the initial condition equal to 1 near each spatial seam while leaving it unchanged on $[-4.5, 4.5]^2$. The observation box is $[-2, 2]^2$ for the single-Dubins, relative-Dubins, and double-integrator cases and $[-3, 3]^2$ for rockets and birds. The prescribed coefficient is

$$\boldsymbol{c}(t, \boldsymbol{x}) = b + 0.04 \cos t \prod_{j=1}^{d} \cos(2\pi \boldsymbol{x}_j / L_j), \qquad b = 0.2, \quad [32]$$

where L_j is the corresponding periodic length. The computation includes its time derivative, gradient, and Laplacian. The sensitivity calculation changes b to 0.35 while keeping the Hamiltonian and initial condition fixed.

Successive refinements can change both spatial resolution and time step; fixed-grid time halving is checked separately. Refinement and solver discrepancies are measured on 65×65 observation points and, in three dimensions, 32 equally spaced headings. These are maximum sampled discrepancies of interpolated fields. Equation residuals use native grid states and spectral spatial derivatives and centered differences at one quarter, one half, and three quarters of the elapsed horizon.

The acceptance thresholds were fixed before the refinement cycle: 0.01 for successive field refinements, 0.02 for the levelset reference (14), 0.002 for time halving and coefficient changes, and 0.005 for each domain-extension test. Sampled original-equation residuals must have maximum at most 0.15 and root-mean-square at most 0.02. The box experiment extends the half-width to 7.5 at fixed spatial spacing and heading resolution; it also changes the time step and coefficient wavelength, so it measures their combined sensitivity. A separate boundary-sensitivity test evolves the original equation on the enlarged box while fixing the time step, spatial spacing, heading count, Hamiltonian, and initial condition on the common domain. This separates boundary sensitivity from changes in the transformation coefficient and time step. Diffusion has infinite propagation speed, so neither finite extension supplies a whole-space boundary-error certificate.

Table 1 separates time-step, coefficient, and domain sensitivity. All comparisons meet their thresholds; these sampled checks do not establish the source iteration's invariant-set hypotheses.

F. Numerical comparison summary.

4. Conclusion

The variable-coefficient Cole–Hopf transformation maps the viscous Hamilton–Jacobi equation to a semilinear heat equation with a complete nonlinear source. Retaining the algebraic and coefficient-derivative terms preserves the original regularized equation under positive logarithmic inversion. The deterministic solvers integrate this transformed equation by Fourier collocation or centered finite differences.

Analytic solutions, refinement studies, coefficient variation, domain extension, and same-viscosity reference fields test the implementation. The rockets, relative-Dubins, single-Dubins, double-integrator, and starling-inspired cases yield maximum sampled reference discrepancies below 3.3×10^{-3} on the reported observation queries. These comparisons validate the stated discretizations on finite periodic boxes. They do not establish whole-space error bounds, dimension-independent complexity, or continuous-state safety certificates.

The 100,000-state experiment evaluates one precomputed three-dimensional relative-state field at independently sampled four-component queries. It demonstrates repeated interpolation of a reduced value field; it does not solve

DRAFT

Table 2. Maximum sampled discrepancies for the `HJ-Gauss` computations. Refinement and `Levelset` Reference columns use the common observation queries; the residual column gives the largest sampled residual over native states. The grid column lists the fine spatial and heading counts.

System	Grid	Refinement	Levelset Reference	Residual
Rockets	$160^2 \times 80$	0.007481	0.003223	0.1433
Dubins vehicles	$224^2 \times 112$	0.005717	0.002511	0.1379
Single Dubins	$128^2 \times 64$	0.009297	0.001415	0.02992
Double integrator	128^2	0.006741	5.60×10^{-4}	0.01187
Bird model	$192^2 \times 96$	0.008817	6.44×10^{-4}	0.1295

a coupled flock game. The associated component, hole, and Euler counts describe thresholded numerical slices. They provide useful geometric diagnostics without implying biological transition laws or invariant barriers.

The source code records the solver settings, refinement checks, residual samples, and archive provenance used for the reported fields. Future work may replace the deterministic grids with a fully reconstructed nonlinear sampling iteration. Such an implementation would require separate evidence for gradient reconstruction, admissibility, accumulated sampling error, and fixed-point stopping.

A. Heat-kernel and potential representations

The transformed equation separates diffusion from a nonlinear source. For a prescribed bounded source f, the heat semigroup gives

$$z(t,\boldsymbol{x}) = \mathbb{E}[z_0(\boldsymbol{x} + \sqrt{\delta t}\, Z)] + \int_0^t \mathbb{E}[f(s, \boldsymbol{x} + \sqrt{\delta(t-s)}\, Z)]\, ds, \qquad Z \sim \mathcal{N}(0, I_n). \tag{A.33}$$

This representation explains the diffusion operator used by the exponential integrator. The reported numerical solvers evaluate the field on deterministic grids; they do not estimate Eq. (A.33) by random sampling.

For $t > 0$, differentiation of the heat kernel yields

$$Dz(t,\boldsymbol{x}) = \frac{\mathbb{E}[Z z_0(\boldsymbol{x} + \sqrt{\delta t}\, Z)]}{\sqrt{\delta t}} + \int_0^t \frac{\mathbb{E}[Z f(s, \boldsymbol{x} + \sqrt{\delta(t-s)}\, Z)]}{\sqrt{\delta(t-s)}}\, ds. \tag{A.34}$$

The singularity at $s = t$ is integrable in the deterministic semigroup bound used in Appendix B. Spectral or finite-difference differentiation supplies the gradients in the experiments.

A prescribed bounded continuous potential R gives a related Feynman–Kac representation. With $X_r = \boldsymbol{x} + \sqrt{\delta} W_r$ for Brownian motion W, the solution of $z_t = \delta \Delta z/2 + Rz$ satisfies

$$z(t,\boldsymbol{x}) = \mathbb{E}_{\boldsymbol{x}}\left[z_0(X_t) \exp\left\{ \int_0^t R(t-r, X_r)\, dr \right\} \right]. \tag{A.35}$$

When R depends on the unknown value and gradient, this formula remains implicit. The deterministic solvers therefore integrate the complete additive source in Eq. (10).

B. Contraction, residual bounds, and robustness

This appendix gives conditional convergence and a residual certificate for the full transformed equation.

A. Convergence of source iteration. Gradient dependence requires a norm that controls both values and first derivatives. Let $\mathrm{BUC}^1(\mathbb{R}^n)$ contain continuously differentiable functions with bounded, uniformly continuous values and gradients. On $X_\tau = C([0,\tau]; \mathrm{BUC}^1)$, use

$$\|z\|_{X_\tau} = \sup_{s \le \tau} \|z(s)\|_\infty + \sup_{s \le \tau} \|Dz(s)\|_\infty. \tag{B.36}$$

For $\boldsymbol{g} \in \mathrm{BUC}^1$ and bounded coefficient derivatives, the transformed initial condition belongs to the same space. Define the mild update by

$$(\mathcal{M}z)(t) = S_t \boldsymbol{\omega}_0 + \int_0^t S_{t-s} F(s, \cdot, z(s), Dz(s))\, ds. \tag{B.37}$$

Theorem B.1 (Conditional finite-time convergence)**.** *Let $\mathcal{A} \subset X_\tau$ be nonempty, closed, and invariant under $\mathcal{M}$. Suppose all its members satisfy $a \le z \le b$ and $|Dz| \le Q$, with $a > 0$. Assume that the source is bounded and uniformly continuous on the relevant coefficient and state ranges, and satisfies*

$$|F(t,\boldsymbol{x},z,q) - F(t,\boldsymbol{x},\widetilde{z},\widetilde{q})| \le L\big(|z-\widetilde{z}| + |q-\widetilde{q}|\big). \tag{B.38}$$

If $\theta = L(\tau + 2\sqrt{n\tau/\delta}) < 1$, then $\mathcal{M}$ has a unique fixed point in $\mathcal{A}$. Its iterates satisfy

$$\|z^{(K)} - \boldsymbol{\omega}\|_{X_\tau} \le \theta^K \|z^{(0)} - \boldsymbol{\omega}\|_{X_\tau}, \qquad \|z^{(K)} - \boldsymbol{\omega}\|_{X_\tau} \le \frac{\theta}{1-\theta} \|z^{(K)} - z^{(K-1)}\|_{X_\tau}. \tag{B.39}$$

for $K \ge 1$. Here finite-time convergence means convergence as $K \to \infty$ on the finite elapsed-time interval $[0,\tau]$; it does not assert termination after finitely many updates. If the fixed point is classical, its inverse solves the original viscous equation.

Proof of Theorems 2.1 and B.1. The space $\mathrm{BUC}^1(\mathbb{R}^n)$ is Banach under the sum of its uniform value and gradient norms. Hence X_τ is Banach, and its closed nonempty subset $\mathcal{A}$ is complete. Invariance makes $\mathcal{M}$ a self-map on this set.

For $z, \widetilde{z} \in \mathcal{A}$, write

$$d(s,\boldsymbol{x}) = F(s,\boldsymbol{x}, z(s,\boldsymbol{x}), Dz(s,\boldsymbol{x})) - F(s,\boldsymbol{x}, \widetilde{z}(s,\boldsymbol{x}), D\widetilde{z}(s,\boldsymbol{x})).$$

The source Lipschitz bound gives $\|d(s)\|_\infty \le L\|z - \widetilde{z}\|_{X_\tau}$ for every $s \in [0,\tau]$. The common initial-condition terms cancel

DRAFT

in $\mathcal{M}z - \mathcal{M}\widetilde{z}$. Since the heat semigroup contracts the uniform norm,

$$\|\mathcal{M}z(t) - \mathcal{M}\widetilde{z}(t)\|_\infty \le \int_0^t \|d(s)\|_\infty \, ds \le Lt\|z - \widetilde{z}\|_{X_\tau}. \tag{B.40}$$

Gaussian differentiation, followed by $\mathbb{E}|Z| \le \sqrt{n}$ for $Z \sim \mathcal{N}(0, I_n)$, yields

$$\|DS_r h\|_\infty \le \frac{\mathbb{E}|Z|}{\sqrt{\delta r}}\|h\|_\infty \le \sqrt{\frac{n}{\delta r}}\|h\|_\infty, \qquad r > 0. \tag{B.41}$$

The singularity at $r = 0$ is integrable. Differentiating the source integral therefore gives

$$\begin{aligned} &\|D\mathcal{M}z(t) - D\mathcal{M}\widetilde{z}(t)\|_\infty \\ &\quad \le L \int_0^t \sqrt{\frac{n}{\delta(t-s)}}\, ds \, \|z - \widetilde{z}\|_{X_\tau} \\ &\quad = 2L\sqrt{\frac{nt}{\delta}}\|z - \widetilde{z}\|_{X_\tau}. \end{aligned} \tag{B.42}$$

Taking the two time suprema and adding proves

$$\|\mathcal{M}z - \mathcal{M}\widetilde{z}\|_{X_\tau} \le L\left(\tau + 2\sqrt{n\tau/\delta}\right)\|z - \widetilde{z}\|_{X_\tau} = \theta\|z - \widetilde{z}\|_{X_\tau}.$$

The assumption $\theta < 1$ and Banach's fixed-point theorem give a unique fixed point $\boldsymbol{\omega} \in \mathcal{A}$. For each starting iterate $z^{(0)} \in \mathcal{A}$, invariance keeps every subsequent iterate in $\mathcal{A}$. Repeated contraction against the fixed point gives the first estimate in Eq. (B.39).

For the posterior estimate, contraction between successive iterates gives

$$\|z^{(K+j+1)} - z^{(K+j)}\|_{X_\tau} \le \theta^{j+1}\|z^{(K)} - z^{(K-1)}\|_{X_\tau}, \qquad j \ge 0.$$

Sum these differences from $j = 0$ to infinity and use convergence to the fixed point. The geometric series has sum $\theta/(1-\theta)$, proving the second estimate. When $\theta = 0$, the map is constant on $\mathcal{A}$ and one update reaches its fixed point.

Finally, $\boldsymbol{\omega} \ge a > 0$ permits logarithmic inversion. If the fixed point is classical, its mild equation implies the full transformed differential equation. Lemma 2.1 then shows that its inverse solves the original viscous equation. □

For bounded coefficient derivatives, $\boldsymbol{c} \ge \boldsymbol{c}_- > 0$, and $z \ge a > 0$, the inverse maps have bounded derivatives on bounded (z, q) ranges. A Hamiltonian uniformly bounded and locally Lipschitz in p on those ranges, uniformly over $(t, \boldsymbol{x})$, therefore supplies a finite source constant L. No convexity assumption is needed for this contraction argument.

The global complexity theorem in (20, Corollary 4.8) does not follow from this local argument. Their setting imposes a globally Lipschitz source in the value and gradient variables, together with strong smoothness and derivative-growth bounds for the complexity result. The transformed source need not meet those assumptions. Even with constant $\boldsymbol{c}$ and the linear Hamiltonian $\boldsymbol{H}(p) = ap$ in one dimension, it becomes

$$F(z, q) = -aq - \frac{\delta}{2z}q^2. \tag{B.43}$$

This source is singular as z approaches zero and is quadratic in q. Using a globally Lipschitz extension to analyze the original equation would require a proof that the solution remains inside the bounded positive region on which the sources agree. Transferring their complexity result would also require verifying their dimension-dependent constants and quadrature regularity. The present contraction theorem establishes neither requirement.

Invariance is a substantive hypothesis. One sufficient construction starts with $b_0(t) = S_t\boldsymbol{\omega}_0$ and an X_τ ball of radius r about b_0. Choose $r < \inf \boldsymbol{\omega}_0$ to preserve positivity. If $|F| \le B_F$ throughout that ball and

$$B_F\left(\tau + 2\sqrt{n\tau/\delta}\right) \le r, \tag{B.44}$$

then the mild map preserves the ball. Under the preceding uniform-in-state Hamiltonian and coefficient assumptions, bounded initial values and gradients give finite source ranges for sufficiently small τ. The case of a constant $\boldsymbol{c} = 1/\delta$ and $\boldsymbol{H} = |p|^2/2$ has $F = 0$ and $\theta = 0$, so the hypotheses include a nonempty solvable case. Extension to a longer horizon requires renewed bounds and invariance on each interval; a global contraction is not asserted.

If $0 < \theta < 1$ and the initial error is bounded by $E_0 > 0$, a sufficient iteration count is

$$K \ge \max\left\{0, \left\lceil \frac{\log(E_0/\varepsilon)}{\log(1/\theta)} \right\rceil\right\}. \tag{B.45}$$

When $\theta = 0$, one update reaches the fixed point. A small change between noisy iterates alone does not certify convergence.

B. Scope of the deterministic implementation. The contraction theorem concerns the whole-interval mild map. The reported solvers instead apply exponential or classical Runge–Kutta time integration after spatial discretization. Their refinement studies measure discretization consistency on the stated periodic boxes. They do not verify the invariant-set hypothesis of Theorem B.1.

The implementation checks positivity at every time step and evaluates equation residuals at selected native-grid states and times. These checks detect numerical failures and support comparisons across refinements. They do not bound the continuum residual between grid states or between sampled times.

C. A posteriori certificate for the original equation. A residual of the full transformed equation measures the residual of the original equation directly. Assume comparison for the original parabolic equation on the whole space. Let U be a bounded classical approximation with bounded residual, and define

$$w = e^{-\boldsymbol{c}U}, \qquad d = w_t - \frac{\delta}{2}\Delta w - F(t, \boldsymbol{x}, w, Dw). \tag{B.46}$$

Theorem B.2 (Residual certificate)**.** *Under these hypotheses, the viscous solution with initial condition $\boldsymbol{g}$ obeys*

$$\|U(t) - \boldsymbol{v}^\delta(t)\|_\infty \le \|U(0) - \boldsymbol{g}\|_\infty + \int_0^t \left\| \frac{d(s)}{\boldsymbol{c}(s)w(s)} \right\|_\infty ds. \tag{B.47}$$

Proof. Lemma 2.1 gives $d = -\boldsymbol{c}wr_U$, with $r_U = U_t + \boldsymbol{H}(t, \boldsymbol{x}, DU) - \delta\Delta U/2$. Let $e_0 = \|U(0) - \boldsymbol{g}\|_\infty$ and $E(t) = e_0 + \int_0^t \|r_U(s)\|_\infty ds$. Since the Hamiltonian does not depend on the value, $U - E$ is a subsolution and $U + E$ is a supersolution. Their initial conditions bracket $\boldsymbol{g}$. Comparison gives $U - E \le \boldsymbol{v}^\delta \le U + E$, proving the bound. □

DRAFT

The source must include both residual components when computing d. If a solver omits $\boldsymbol{R}_{\mathrm{der}}$, then its transformed residual contains the missing term $-w\boldsymbol{R}_{\mathrm{der}}$. The certificate charges that omission. Residuals evaluated only at sampled states are diagnostic; rigorous use requires a bound between those states and through time, including derivative approximation error.

D. Viscosity, model perturbations, and level sets. Vanishing viscosity remains a separate approximation. Suppose the Hamiltonian and initial condition satisfy a comparison and approximation theorem giving $\|\boldsymbol{v}^{\delta} - \boldsymbol{v}^{0}\|_{\infty} \le C_{\mathrm{vis}}\sqrt{\delta}$ on the chosen horizon. This rate is an additional hypothesis, rather than a consequence of the transformation. Under the same uniform norm and domain, Theorem B.2 then gives

$$\|U(t) - \boldsymbol{v}^{0}(t)\|_{\infty} \le \|U(0) - \boldsymbol{g}\|_{\infty} + \int_0^t \left\| \frac{d(s)}{\boldsymbol{c}(s)w(s)} \right\|_{\infty} ds + C_{\mathrm{vis}}\sqrt{\delta}. \quad [B.48]$$

Proposition B.1 (Hamiltonian and initial condition perturbations)**.** *Suppose two equations with the same diffusion admit comparison, their initial conditions differ by at most ϵ_g, and $|\boldsymbol{H}_1(t,\boldsymbol{x},p) - \boldsymbol{H}_2(t,\boldsymbol{x},p)| \le \epsilon_H$ throughout the required co-state range. For classical solutions, it suffices that this range contains $D\boldsymbol{v}_2$. Then*

$$\|\boldsymbol{v}_1(t) - \boldsymbol{v}_2(t)\|_{\infty} \le \epsilon_g + t\epsilon_H. \quad [B.49]$$

Proof. The functions $\boldsymbol{v}_2 - \epsilon_g - t\epsilon_H$ and $\boldsymbol{v}_2 + \epsilon_g + t\epsilon_H$ are a subsolution and a supersolution for the first equation. Comparison proves the claim. For viscosity solutions, impose the Hamiltonian bound on the test-gradient range required by comparison, or uniformly over all p. □

Changing a prescribed positive transformation coefficient does not perturb the Hamiltonian when both source components are retained. Thus a smooth positive regularization that preserves the stated differentiability changes coordinates; it creates no Hamiltonian modeling error by itself. Hard clipping can destroy that differentiability and falls outside these classical results. If the Hamiltonian is deliberately replaced, the perturbation bound applies to that separate change. The matching choice $\boldsymbol{c} = 2\boldsymbol{H}(t,\boldsymbol{x},D\boldsymbol{v})/(\delta|D\boldsymbol{v}|^2)$ can vanish, change sign, or become singular. At $\boldsymbol{c} = 0$, the exponential transform loses the value information. Recomputing this ratio also requires regularity beyond the prescribed-coefficient hypotheses. `HJ-Gauss` permits a positive constant coefficient even in these cases.

If a uniform bound $|U - \boldsymbol{v}^{0}| \le E$ has been established on a specified domain, then

$$\{U < -E\} \subseteq \{\boldsymbol{v}^{0} < 0\}, \qquad \{U > E\} \subseteq \{\boldsymbol{v}^{0} > 0\}. \quad [B.50]$$

Proof of Corollary 2.3. Fix a point in the specified set and suppress its arguments. The assumed error bound is equivalent to

$$U - E \le \boldsymbol{v}^{0} \le U + E. \quad [B.51]$$

If $U > E$, then the lower bound gives $\boldsymbol{v}^{0} \ge U - E > 0$. Thus the point lies outside the target-reaching class $\{\boldsymbol{v}^{0} \le 0\}$. If $U < -E$, then the upper bound gives $\boldsymbol{v}^{0} \le U + E < 0$, placing the point in the strict negative sublevel set. Since the argument applies at every point covered by the error bound, it proves both inclusions in Eq. (B.50).

The states assigned neither strict sign by this rule satisfy $-E \le U \le E$, which is the abstention band $|U| \le E$. At its boundaries, the corresponding estimate in Eq. (B.51) is nonstrict, so the corollary makes no strict sign assertion there.

If the assumed error bound holds simultaneously on an event of probability at least $1 - \eta$, both sign implications hold simultaneously on that same event. No additional union bound is needed. The domain of the sign certificate is the domain on which that error bound has been established; a bound at finitely many queries supplies no assertion between those queries. □

Interpreting either sign as safety also requires the corresponding game's value convention and, for reach–avoid problems, a correctly solved obstacle problem.

Data, Materials, and Software Availability

The deterministic transformed-PDE solvers, reference computations, numerical records, and rendering scripts are available at https://github.com/robotsorcerer/levelsetpy/tree/main/levelsetpy/monte_carlo. Companion animations are available at https://scriptedonachip.com/downloads/Papers/assets/anim/.

1. M Althoff, G Frehse, A Girard, Set Propagation Techniques for Reachability Analysis. *Annu. Rev. Control. Robotics, Auton. Syst.* **4**, 369–395 (2021).
2. JP Aubin, AM Bayen, P Saint-Pierre, *Viability Theory*. No. August 2015, (2011).
3. KL Hobbs, ML Mote, MC Abate, SD Coogan, EM Feron, Runtime assurance for safety-critical systems. *IEEE Control. Syst. Mag.* **43**, 28–65 (2023).
4. Defense Acquisition University, Verification (2023) Accessed April 5, 2023.
5. C Livadas, NA Lynch, Formal verification of safety-critical hybrid systems in *International Workshop on Hybrid Systems: Computation and Control*. (Springer), pp. 253–272 (1998).
6. CJ Tomlin, J Lygeros, SS Sastry, A game theoretic approach to controller design for hybrid systems. *Proc. IEEE* **88**, 949–970 (2000).
7. I Mitchell, A Robust Controlled Backward Reach Tube with (Almost) Analytic Solution for Two Dubins Cars. *EPiC Series in Computing* **74**, 242–258 (2020).
8. R Isaacs, Differential Games: A Mathematical Theory with Applications to Warfare and Pursuit, Control and Optimization. (1966).
9. MG Crandall, LC Evans, PL Lions, Some Properties of Viscosity Solutions of Hamilton-Jacobi Equations. *Transactions Am. Math. Soc.* **282**, 487 (1984).
10. IM Mitchell, AM Bayen, CJ Tomlin, A Time-Dependent Hamilton-Jacobi Formulation of Reachable Sets for Continuous Dynamic Games. *IEEE Transactions on Autom. Control.* **50**, 947–957 (2005).
11. S Osher, CW Shu, High-Order Essentially Nonoscillatory Schemes for Hamilton-Jacobi Equations. *SIAM J. Numer. Analysis* **28**, 907–922 (1991).
12. MG Crandall, A Majda, Monotone Difference Approximations For Scalar Conservation Laws. *Math. Comput.* **34**, 1–21 (1980).
13. S Osher, R Fedkiw, Level Set Methods and Dynamic Implicit Surfaces. *Appl. Mech. Rev.* **57**, B15–B15 (2004).
14. L Molu, LevelSetPy: A GPU-Accelerated Package for Hyperbolic Hamilton-Jacobi Partial Differential Equations' Solubility. *The ACM Transactions on Math. Softw.* (2025).
15. L Molu, The Python LevelSet Toolbox (LevelSetPy) in *2024 IEEE 63rd Conference on Decision and Control (CDC)*. pp. 8938–8945 (2024).
16. L Evans, PE Souganidis, Differential Games And Representation Formulas For Solutions Of Hamilton-Jacobi-Isaacs Equations. *Indiana Univ. Math. J* **33**, 773–797 (1984).
17. S Osher, JA Sethian, Fronts Propagating with Curvature-Dependent Speed: Algorithms based on Hamilton-Jacobi Formulations. *Journal of Computational Physics* **79**, 12–49 (1988).
18. J Lygeros, On reachability and minimum cost optimal control. *Automatica* **40**, 917–927 (2004).
19. MG Crandall, PL Lions, Viscosity solutions of hamilton-jacobi equations. *Transactions Am. mathematical society* **277**, 1–42 (1983).
20. M Hutzenthaler, T Kruse, Multilevel Picard Approximations of High-Dimensional Semilinear Parabolic Differential Equations with Gradient-Dependent Nonlinearities. *SIAM J. on Numer. Analysis* **58**, 929–961 (2020).
21. MG Crandall, PL Lions, Two Approximations of Solutions of Hamilton-Jacobi Equations. *Mathematics of Computation* **43**, 1–19 (1984).
22. SP Bhat, DS Bernstein, Continuous finite-time stabilization of the translational and rotational double integrators. *IEEE Transactions on automatic control* **43**, 678–682 (1998).
23. WM Wonham, Linear multivariable control: A geometric approach. *Appl. Math.* **10** (1985).
24. SE Dreyfus, Control Problems With Linear Dynamics, Quadratic Criterion, and Linear Terminal Constraints, (Rand Corp, Santa Monica Calif), Technical report (1966).
25. R Isaacs, *Differential Games: A Mathematical Theory with Applications to Warfare and Pursuit, Control and Optimization.* (Kreiger, Huntigton, NY), (1999).
26. A Merz, The game of two identical cars. *J. Optim. Theory Appl.* **9**, 324–343 (1972).

DRAFT